Steel and Composite Structures, *Vol. 20, No. 6 (2016) 1323-1343*
DOI: http://dx.doi.org/10.12989/scs.2016.20.6.1323

Numerical studies on behaviour of bolted ball-cylinder joint under axial force

Xiaonong Guo [1], Zewei Huang [1], Zhe Xiong [*1], Shangfei Yang [1] and Li Peng [2]

[1] *Department of Building Engineering, Tongji University, Shanghai 200092, China*
[2] *Shanghai T&D Architechral Technology Co., Ltd., Shanghai 200092, China*

(*Received November 10, 2015, Revised December 30, 2015, Accepted February 16, 2016*)

Abstract. This paper presents the results of an extensive numerical analysis program devoted to the investigation of the mechanical behaviour of bolted ball-cylinder joints. The analysis program is developed by means of finite element (FE) models implemented in the non-linear code ABAQUS. The FE models have been accurately calibrated on the basis of available experimental results. It is indicated that the FE models could be used effectively to describe the mechanical performance of bolted ball-cylinder joints, including failure modes, stress distributions and load-displacement curves. Therefore, the proposed FE models could be regarded as an efficient and accurate tool to investigate the mechanical behavior of bolted ball-cylinder joints. In addition, to develop a further investigation, parametric studies were performed, varying the dimensions of hollow cylinders, rectangular tubes, convex washers and ribbed stiffener. It is found that the dimensions of hollow cylinders, rectangular tubes and ribbed stiffener influenced the mechanical behaviour of bolted ball-cylinder joints significantly. On the contrary, the effects of the dimensions of convex washers were negligible.

Keywords: bolted ball-cylinder joints; FE models; failure modes; parametric studies; mechanical behaviour

1. Introduction

For the time being, the concept of advanced space truss structures has been focused on seeking more efficient joints. The bolted ball-cylinder joint which belongs to an innovative joint system has a favourable application potential in space truss structures. Rectangular tubes are selected for the upper chord members of the novel space truss structure with bolted ball-cylinder joints. A typical ball-cylinder node consists of a hollow cylinder with an opening welded to a solid hemisphere. This hollow cylinder can be connected to the upper chord members tightly and rapidly by high strength bolts. The detailed information of the bolted ball-cylinder joint was introduced in the companion paper. Due to the better bending resistance of the rectangular tubes, roof boards can be placed at the upper chord members of the novel space truss structure with bolted ball-cylinder joints directly. Therefore, compared with the traditional space truss structure, purlines can be removed in the novel space truss structure with bolted ball-cylinder joints. As a result, three excellent merits can be achieved for the novel space truss structure with bolted ball-cylinder joints:

*Corresponding author, Doctor, E-mail: 123superpanda@tongji.edu.cn

http://www.techno-press.org/?journal=scs&subpage=6 ISSN: 1229-9367 (Print), 1598-6233 (Online)

(1) considerable cost savings; (2) better illuminative effects; (3) ease and rapidness of construction.

Tremendous efforts have been devoted to the mechanical behaviour of traditional joints such as bolt-ball joints (Ghasemi *et al*. 2010, Ebadi *et al*. 2012, Lopez *et al*. 2007, Fan *et al*. 2012, Ma *et al*. 2013), tubular joints (Hyde and Leen 1997, Leen and Hyde 2000, Qiu and Zhao 2009, Lesani *et al*. 2013, Wang *et al*. 2000), etc. Their experimental and theoretical achievements are advanced and developed. Recently, more and more attention has been attracted to the development of the innovative joint, involving aluminium alloy gusset joints (Guo *et al*. 2015a, b, 2016b), bird-beak joints (Chen *et al*. 2015, Pena and Chacon 2014, Cheng *et al*. 2015), composite joints (Loh *et al*. 2006a, b, Thai and Uy 2015), bolted ball-cylinder joints, etc. Guo *et al*. (2015a, b, 2016b) have conducted a series of tests and finite element (FE) models on the mechanical characteristics of aluminium alloy gusset joints. According to experimental and FE results, the formulae to estimate the bending stiffness and bearing capacity of aluminium alloy gusset joints were derived. Experimental investigations and FE analyses on the behaviour of bird-beak X-joints under in-plane bending were performed by Chen *et al*. (2015). Pena and Chacon (2014) and Cheng *et al*. (2015) have explored the behaviour of bird-break joints by means of the numerical analysis. Based on the numerical results, a design proposal aimed at predicting the bearing capacity of bird-beak joints was given. Loh *et al*. (2006a, b) carried out experimental studies on composite flush end plate joints to investigate the effects of partial shear connections. For the further study, Thai and Uy (2015) developed detailed three-dimensional FE models of blind bolted composite joints. However, compared with these aforementioned joints, studies on the behaviour of bolted ball-cylinder joints is few. This limitation will obstruct the development and application of bolted ball-cylinder joints notably.

It can be observed that the joint mechanical behaviour is primarily investigated via experimental tests, FE simulations and theoretical studies. Based on experimental results, a preliminary understanding on the joint mechanical behaviour can be obtained. According to the theoretical studies, a design method for the development and application of the joints can be proposed. However, it will bring huge economical cost to provide numerous experimental data for the theoretical studies. Hence, the FE simulations which act as a link between the experimental tests and the theoretical studies are indispensable. Due to the availability of the powerful FE software packages ABAQUS and ANSYS, the FE simulations have been currently considered to be a more appropriate method to find more information about the joint behaviour. Qiang *et al*. (2014) presented numerical studies on the high strength steel endplate connections under fire conditions for the further information and understanding of their mechanical behaviour. Gil and Bayo (2008) implemented the FE models which are used to simulate the composite joints in the ABAQUS software and calibrated their reliability with experimental results. Based on the FE models, an alternative design for the composite joints was proposed. Pearson and Mottram (2012) carried out a FE modelling methodology for the non-linear stiffness evaluation of adhesively bonded single lap-joints. In general, the FE simulations which can deal with a wide range of engineering problems have become an efficient and accurate tool to investigate the joint mechanical behavior.

The main objective of this paper is to establish a reliable and robust FE model for the further investigation of the mechanical behaviour of bolted ball-cylinder joints. A detail description of the FE models which are conducted via the commercial package ABAQUS is reported. To achieve reliable FE results, all the joint components and the interactions between them are taken into account. The FE models are adjusted, compared and validated with experimental results. Finally, parametric studies are performed by using the proposed FE models, varying the dimensions of hollow cylinders, rectangular tubes, convex washers and ribbed stiffener.

2. FE simulations

The general purpose FE software package ABAQUS 6.11 was used for the numerical investigation of the mechanical behaviour of bolted ball-cylinder joints.

2.1 Geometrical dimensions

The bolted ball-cylinder joint mainly consists of a solid hemisphere, a hollow cylinder, rectangular tubes, concave endplates, high strength bolts, convex washers and ribbed stiffener. To achieve an acceptable level of accuracy, all the components were taken into account in the FE models, as shown in Fig. 1. The geometrical dimensions of all the FE models implemented in the FE software package ABAQUS were the same as those of the bolted ball-cylinder joint specimens reported in the companion paper. Since the geometry of the bolted ball-cylinder joint was symmetric at both two principal axes, only one fourth of this joint was modelled in order to achieve better computational efficiency. The welding material used for rectangular tubes with endplates had the same strength as those corresponding components. Moreover, the study was mainly focused on the bolted connection. Therefore, the welds were not considered in the FE models. To simulate the constraint of the actual loading schemes applied in the tests, the compression plate and the tension plate were employed. The rectangular tube and the concave endplate were assembled and merged together as continuous, assuming perfect weld between parts.

2.2 Selection of the element type and mesh generation

The numerical analyses were extremely sensitive to the selection of the element type and mesh generation. The primary reasons for this are that (1) there were many surface-to-surface contact interactions in the FE models; (2) the nonlinear material properties were taken into consideration; (3) lots of components had the curved surface. Therefore, a suitable element type needed to be selected for the FE models to obtain reliable results. All the components of the bolted ball-cylinder joint have been mainly meshed by eight-node linear brick elements with full integration and incompatible modes (C3D8I). The C3D8I element is developed from the C3D8 element. The C3D8I element brings less computational cost in analyzing bending-dominated problems. The deformation of the ball-cylinder is mainly controlled by the bending moment generated from the axial force. Hence, the C3D8I element is suitable for representing the mechanical behaviour of the bolted ball-cylinder joint in the numerical analyses.

Convergence studies were conducted to obtain the optimum and effective finite element mesh density which provided reliable results with less computational time. All the components were meshed in hex-dominated shape by means of sweep technique following a medial axis algorithm. The mesh generation adopted for all joint components is shown in Fig. 1 with an element size range from 2 mm to 6 mm. To capture a high stress gradient, the fine mesh was created at the region around the ball-cylinder node, whereas the coarse mesh was created at the region away from the ball-cylinder node to save the computational cost. In addition, the intensive mesh was created in the vicinity of bolt holes. The FE model for each bolted ball-cylinder joint contained approximately 13,000 elements.

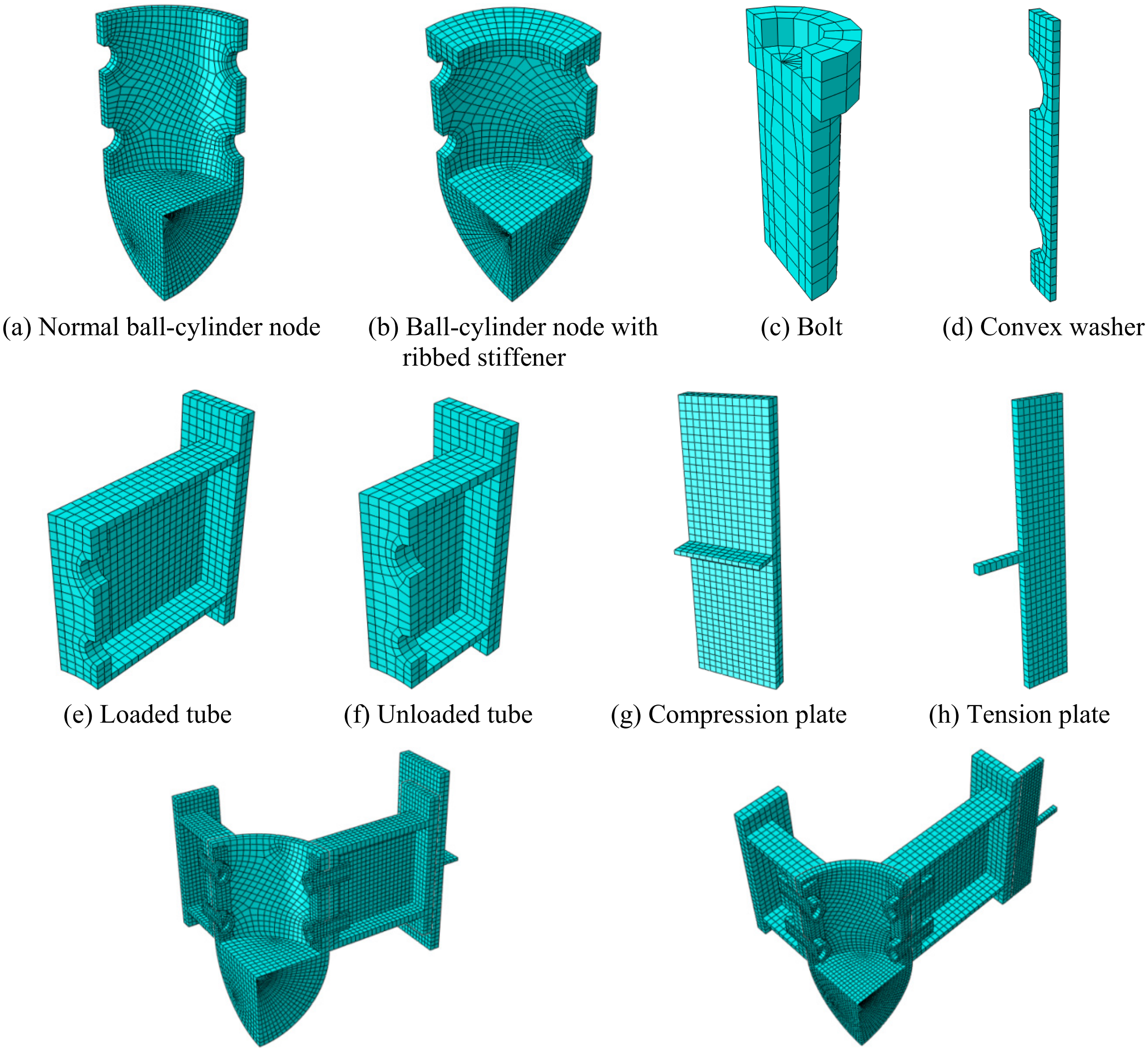

(a) Normal ball-cylinder node (b) Ball-cylinder node with ribbed stiffener (c) Bolt (d) Convex washer

(e) Loaded tube (f) Unloaded tube (g) Compression plate (h) Tension plate

(i) Bolted ball-cylinder joint under compressive load (j) Bolted ball-cylinder joint under tensile load

Fig. 1 FE models

2.3 Material properties

A nonlinear analysis was performed in the FE models through taking both the material and geometric nonlinearities into consideration. A bilinear elastic–plastic model (Fig. 2) based on the elastic modulus and post-yield tangential modulus was developed to simulate the inelastic behaviour of the ball-cylinder node, rectangular tube and washer. When the joint specimens collapsed, the high strength bolts still presented the elastic behaviour. Thereby, to save the computational cost, the bolt was assigned the material elasticity with a Young’s modulus E=206 kN/mm^2 and a Poisson’s coefficient v = 0.3. Both the compression plate and the tension plate were regarded as rigid elements with a large Young's modulus E = 206000 kN/mm^2. The material properties of the ball-cylinder node were obtained from the tensile tests presented in the

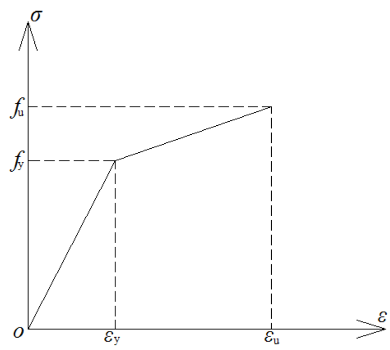

Fig. 2 Bilinear elastic–plastic model

companion paper, while the material properties of the rectangular tube and washer (mild steel *Q*235) were obtained according to the Chinese code for design of steel structures (GB 50017 2003). The von Mises yield criterion was adopted for the estimation of failure.

It is worth pointing out that the material properties obtained for the tensile test were the engineering stress and strain. However, the true stress and plastic strain were required in the FE modelling. The true stress and plastic strain can be calculated by Eqs. (1)~(3). For example, the yield strength f_y and the ultimate tensile strength f_u obtained from the tensile tests were taken as 215.67 MPa and 449.73 MPa, respectively. Hence, according to Eqs. (1)~(3), the true yield strength $f_{y,\mathrm{true}}$ and the ultimate tensile strength $\mathrm{f}_{\mathrm{u,true}}$ were 215.89 MPa and 536.98 MPa, respectively.

$$\sigma_{\mathrm{true}} = \sigma_{\mathrm{eng}}(1+\varepsilon_{\mathrm{eng}}) \tag{1}$$

$$\varepsilon_{\mathrm{true}} = \ln(1+\varepsilon_{\mathrm{eng}}) \tag{2}$$

$$\varepsilon_{\mathrm{pl,\ true}} = \varepsilon_{\mathrm{true}} - \frac{\sigma_{\mathrm{true}}}{E} \tag{3}$$

where σ_{true} represents the true stress; σ_{eng} represents the engineering stress obtained from the tensile tests; $\varepsilon_{\mathrm{eng}}$ represents the engineering strain obtained from the tensile tests; $\varepsilon_{\mathrm{true}}$ represents the true strain; $\varepsilon_{\mathrm{pl,\ true}}$ is the true plastic strain; E is the elastic modulus.

2.4 Contact interactions and constraint conditions

The general contact interactions and constraint conditions which are available in the software package ABAQUS were employed to fully transfer the force between the contacting components. Seven important kinds of contact pairs (Fig. 3) were defined in the FE models: (1) concave endplate-to-hollow cylinder; (2) washer-to-hollow cylinder; (3) nut-to-washer; (4) bolt shank-to-hole of washer; (5) bolt shank-to-hole of hollow cylinder; (6) bolt shank-to-hole of concave endplate in the tension joint; (7) loading plate-to-compression plate. To improve the analysis time, in the compression joint the bolt shank was tied to the hole of concave endplate by the tie constraint. Since the tension plate and loaded tube were welded together, the tie constraint was also used to model the interaction between them, as illustrated in Fig. 4.

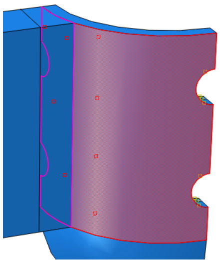
(a) Concave endplate-to-hollow cylinder

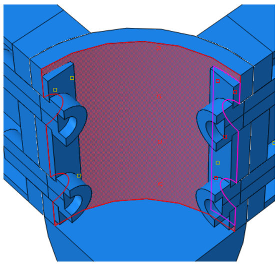
(b) Washer-to-hollow cylinder

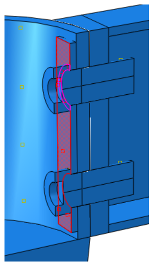
(c) Nut-to-washer

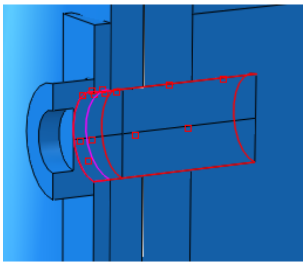
(d) Bolt shank-to-hole of washer

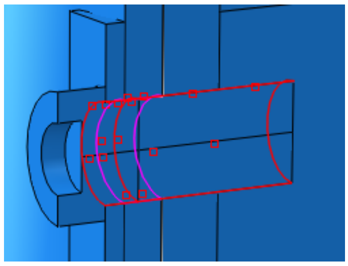
(e) Bolt shank-to-hole of hollow cylinder

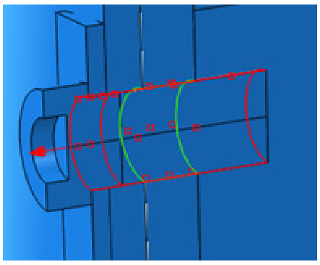
(f) Bolt shank-to-hole of concave endplate

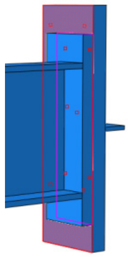
(g) Loading plate-to-compression plate

Fig. 3 Contact pairs of FE models

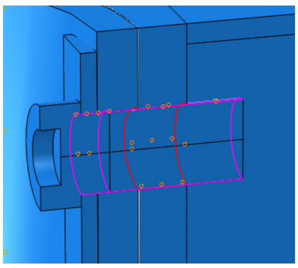
(a) Bolt shank-to-hole of concave endplate

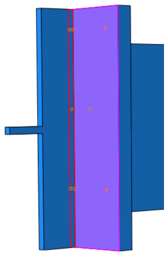
(b) Loading plate-to-tension plate

Fig. 4 Tie constraints of FE models

Surface-to-surface contact based on the small sliding formulation was selected for all contact surfaces. The master and slave surfaces of the contact pairs and the tie constraints are listed in Table 1. The normal interaction between contacting surfaces was defined as hard contact, which allows the surfaces to separate under the effect of tensile force and does not allow penetrating each

Table 1 Characteristics of contact pairs and tie constraints

Contact or constraint	Master surface	Slave surface
Concave endplate-to-hollow cylinder	Hollow cylinder	Concave endplate
Washer-to-hollow cylinder	Hollow cylinder	Washer
Nut-to-washer	Washer	Nut
Bolt shank-to-hole of washer	Bolt shank	Hole of washer
Bolt shank-to-hole of hollow cylinder	Bolt shank	Hole of hollow cylinder
Bolt shank-to-hole of concave endplate (compression joint)	Hole of concave endplate	Bolt shank
Bolt shank-to-hole of concave endplate (tension joint)	Bolt shank	Hole of concave endplate
Loading plate-to-compression plate	compression plate	Loading plate
Loading plate-to-tension plate	tension plate	Loading plate

other under the effect of compressive force. For the tangential behavior, the penalty friction with friction coefficient 0.2 was applied. It is found that the evulsion of the bolt might occur at the tension joint. Therefore, the effect of screw thread between the bolt shank and the hole of concave endplate cannot be neglected for the tension joint. To improve the computational efficiency, the screw thread was replaced by the properties of the bolt shank-to-hole of concave endplate contact. Consequently, an initial clearance of computing for single-threaded bolt was adopted. The half-thread angle was 30 degrees, the screw pitch was 1.5 mm and the bolt diameter was 20 mm.

2.5 Analysis steps and loads

Actually, the high strength bolts were tightly screwed into the rectangular tubes through a large torsion, resulting in the generation of bolt pretension force. To establish the contact interactions and the bolt pretension force stably, six steps were developed in the whole analysis process:

(1) Firstly, the ball-cylinder node, washers and rectangular tubes were fixed of all degrees of freedom temporarily, as shown in Fig. 5. Meanwhile, a very small bolt load 10 N was applied to every bolt.
(2) Secondly, all the temporary restraints were removed.
(3) Thirdly, a small axial displacement 0.001 mm was located at the compression or tension plate, as shown in Fig. 6. After these three steps, the contact interactions have been generated smoothly and successfully.
(4) Fourthly, the value of the bolt load was modified as 5000 N, which is regarded as the true bolt pretension force.
(5) Subsequently, the method “apply force” was change to “fix at current length” in the bolt load option. In this step, the deformation caused by the bolt pretension force was remained. And in the following step, the bolt stress will change with the action of other force or displacement.
(6) Finally, the axial displacement (established in the third step) was modified as a larger value so that the joint model can be collapsed. In this final step, a nonlinear analysis which takes the arc-length method as the convergence algorithm was carried out.

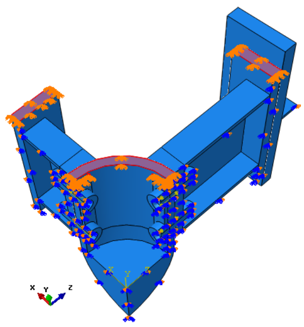

Fig. 5 Temporary restraints

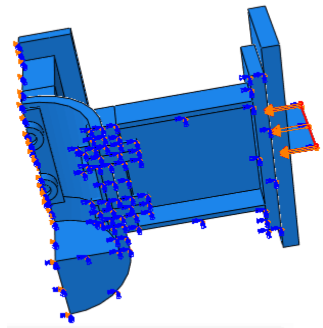

Fig. 6 Displacement load

2.5 Analysis steps and loads

Actually, the high strength bolts were tightly screwed into the rectangular tubes through a large torsion, resulting in the generation of bolt pretension force. To establish the contact interactions and the bolt pretension force stably, six steps were developed in the whole analysis process:

(1) Firstly, the ball-cylinder node, washers and rectangular tubes were fixed of all degrees of freedom temporarily, as shown in Fig. 5. Meanwhile, a very small bolt load 10 N was applied to every bolt.

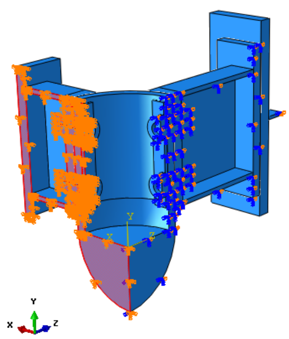

(a) Symmetric boundary conditions for the *x*-*y* plane

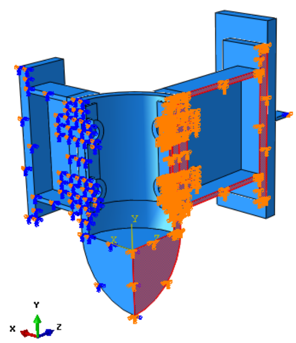

(b) Symmetric boundary conditions for the *z*-*y* plane

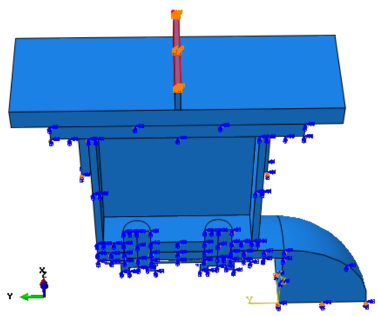

(c) Boundary conditions at end of the compressive or tension plate

Fig. 7 Boundary conditions

(2) Secondly, all the temporary restraints were removed.
(3) Thirdly, a small axial displacement 0.001 mm was located at the compression or tension plate, as shown in Fig. 6. After these three steps, the contact interactions have been generated smoothly and successfully.
(4) Fourthly, the value of the bolt load was modified as 5000 N, which is regarded as the true bolt pretension force.
(5) Subsequently, the method “apply force” was change to “fix at current length” in the bolt load option. In this step, the deformation caused by the bolt pretension force was remained. And in the following step, the bolt stress will change with the action of other force or displacement.
(6) Finally, the axial displacement (established in the third step) was modified as a larger value so that the joint model can be collapsed. In this final step, a nonlinear analysis which takes the arc-length method as the convergence algorithm was carried out.

3. Verifications of FE models

It is necessary to verify the validity and reliability of the FE models of bolted ball-cylinder joints. The bolted ball-cylinder joint specimens which were recently tested were simulated and the numerical results were compared with the test results. The comparisons concerned failure modes, stress distributions and load-displacement curves.

3.1 Failure modes

The comparisons on the failure modes and final deformation states of the bolted ball-cylinder joint specimens between FE simulations and experimental results are investigate in Figs. 8-12. Moreover, Figs. 8-12 show the numerical contour plots of Mises stress, as this is the effective way to determine failure position. The observations were found as follows:

(1) Fig. 8 presents the comparisons of the failure modes of the bolted ball-cylinder joint JD1. It can be found that the numerical modelling was in line with the experimental results. The FE model reasonably predicted the failure modes of the bolted ball-cylinder joint due to the separation between the hollow cylinder and the concave endplate of the unloaded tube and the indentation of the hollow cylinder at the region connected with the loaded tube. Although the FE model cannot simulate the indentation of the hollow cylinder, it was able to reveal the location where the Mises stress reached its ultimate strength. In addition, the deformation at the hollow cylinder opening was extremely large, while the deformation of the hollow cylinder near the solid hemisphere was relative small. The deformation matched the experimental results obtained from the companion paper. Similar observations could be found for the joints JD2 and JD3.
(2) Fig. 9 plots the comparisons of the failure modes of the bolted ball-cylinder joint JD4. The height of the hollow cylinder was short so that the deformation near the solid hemisphere was limited significantly. Therefore, the Mises stress was very large at the position near the solid hemisphere, which implied the punching damage. The calculation absorbed when the punching damage occurred. Hence, the final deformation of the joint JD4 was relative small. The coincidence between the test and the FE simulation could be regarded as fairly good.

(3) Fig. 10 shows the comparisons on the final deformation states of the bolted ball-cylinder joint JD5 and its components after failure. The findings of the joint JD5 was similar to that of the joint JD1. It is worth noting that the warping of the ribbed stiffener caused by the compressive load was also simulated in the FE model.

(4) The comparisons on the failure modes of the FE model and the test specimen JD7 are shown in Fig. 11. The FE failure mode was exactly the same with the experimental one, signifying that good agreement existed on the failure mode of the joint JD7. The contact surface between the hollow cylinder and the concave endplate of the loaded tube separated due to the tensile force, and the gap increased with the increase of tensile force. Although the FE model cannot simulate the weld cracking, the evulsion of the bolt could be judged according to the large deformation and Mises stress at the bolt holes.

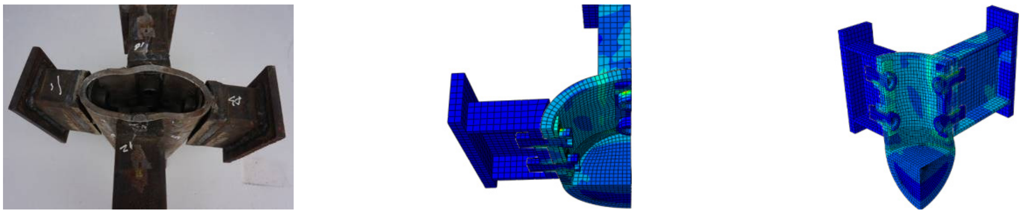

(a) Deformation

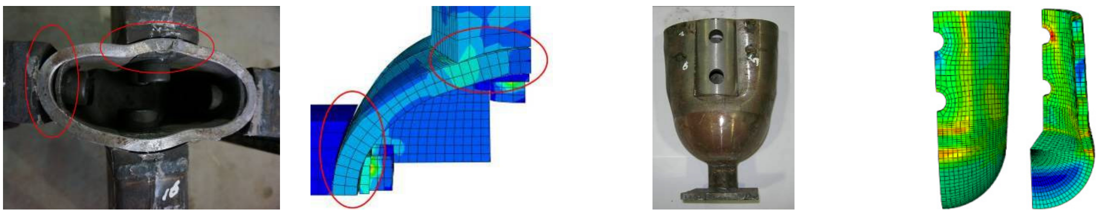

(b) Separation (c) Indentation

Fig. 8 Failure modes of the joint specimen JD1

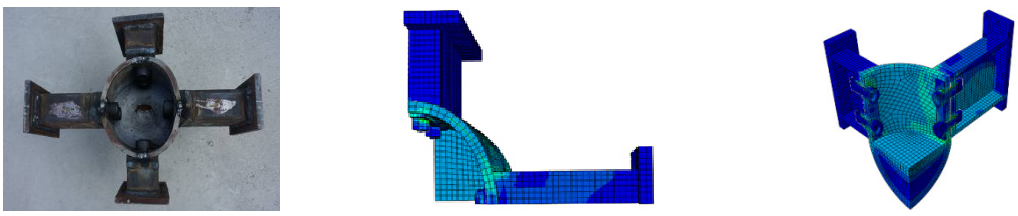

(a) Deformation

(b) Punching failure

Fig. 9 Failure modes of the joint specimen JD4

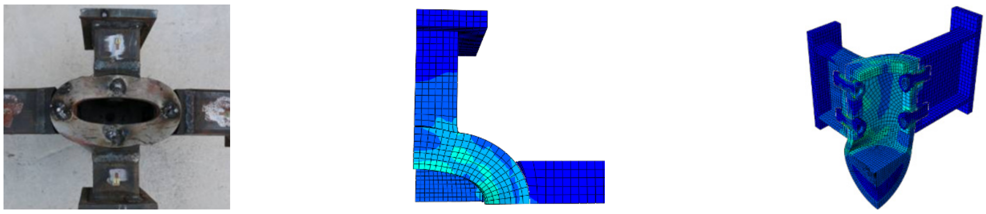

(a) Deformation

(b) Flat (c) Warping of the ribbed stiffener

Fig. 10 Failure modes of the joint specimen JD5

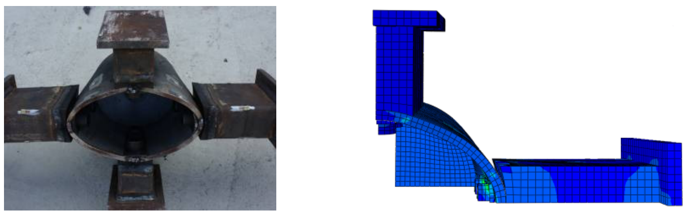

(a) Deformation

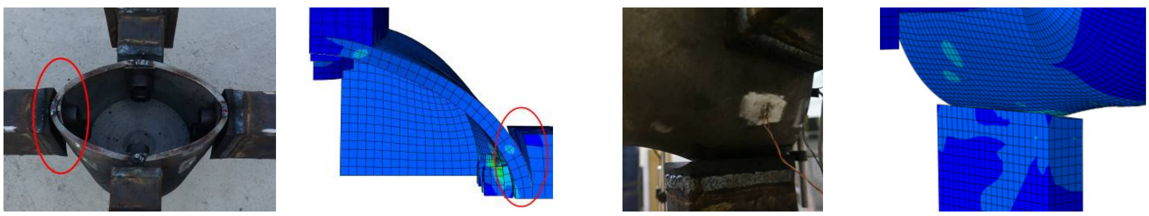

(b) Separation (c) Evolution of the bolts

Fig. 11 Failure modes of the joint specimen JD7

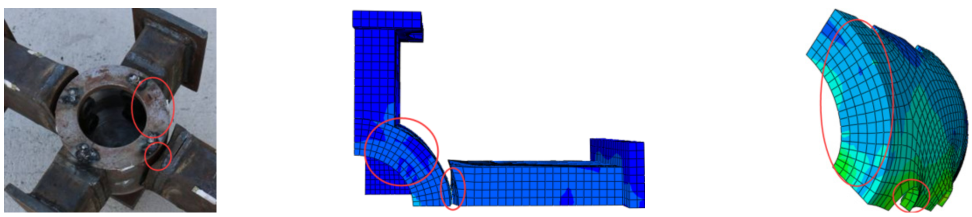

(a) (b) (c)

Fig. 12 Failure modes of the joint specimen JD8

(5) Fig. 12 illustrates the comparisons of the failure mode of the bolted ball-cylinder joint JD8. It is shown that the FE results agreed well with the test results. The contact surface between the hollow cylinder and the concave endplate of the loaded tube separated due to the tensile force. The deformation at the hollow cylinder opening was inconspicuous, which demonstrated that the ribbed stiffener improved the stiffness of the bolted ball-cylinder joint.

Concerning the failure modes, it can be noted that the proposed FE models were able to describe the behaviour of bolted ball-cylinder joints with sufficient accuracy.

3.2 Stress distributions

The compressive force was transferred to the hollow cylinder by the concave endplate-to-hollow cylinder contact pair, while the tensile force was transferred to the hollow cylinder by the bolt shank-to-hole of concave endplate, nut-to-washer and washer-to-hollow cylinder contact pairs. The theoretical models of the bolted ball-cylinder joint under compressive force and tensile force are simplified in Figs. 13(a) and 13(b), respectively. According to the theory of structural mechanics (Bao and Gong 2006), bending moments acting on one fourth of the hollow cylinder could be obtained, as plotted in Fig. 13. For the compression joint, the hollow cylinder contacted with the concave endplate of the loaded tube tightly, leading to an effective constraint of the concave endplate, and the positive bending moment was generated at this point; while the hollow cylinder was separated from the concave endplate of the unloaded tube, resulting in an ineffective constraint of the concave endplate, and the negative bending moment was generated at this point. The conclusion of the tension joint was opposite to that of the compression joint.

The stress distributions of the bolted ball-cylinder joint could be obtained by means of the proposed numerical simulations. The contour plots of the equivalent pressure stress on the hollow cylinder opening are shown in Fig. 14. The equivalent pressure stress p is defined as

$$p = -\frac{1}{3}\left(\sigma_{11} + \sigma_{22} + \sigma_{33}\right) \tag{4}$$

Where σ_{11}, σ_{22} and σ_{33} represent the components of stress. $p > 0$ means the compressive stress, while $p < 0$ means the tensile stress. It could be easily deduced that (1) for the compression joint, the positive bending moment was created at the area of the hollow cylinder connected with the loaded tube, and the negative bending moment was created at the area of the hollow cylinder connected with the unloaded tube; (2) for the tension joint, its bending moment distribution was opposite to that of the compression joint.

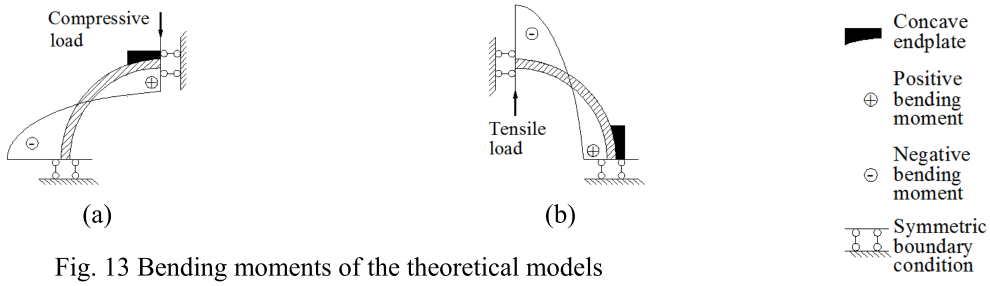

Fig. 13 Bending moments of the theoretical models

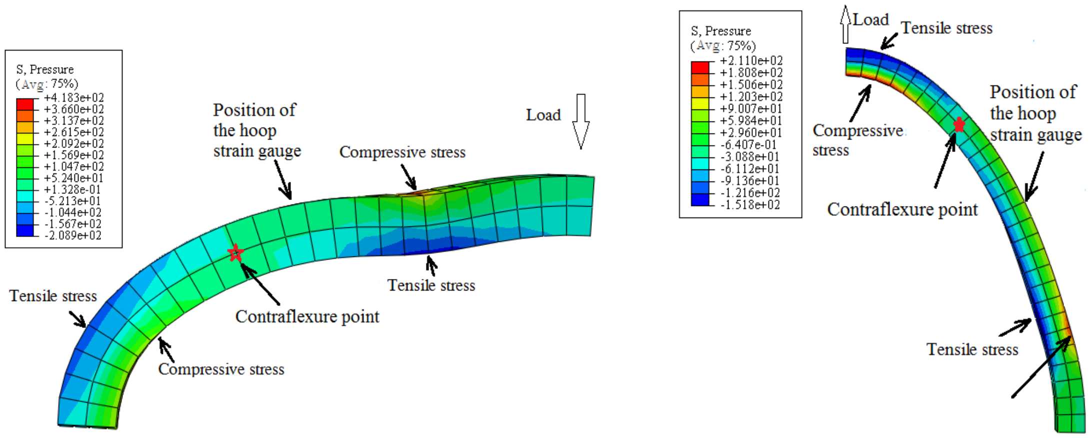

(a) JD1 (b) JD7

Fig. 14 Equivalent pressure stress on the hollow cylinder opening

The stress distributions of the numerical simulations and the theoretical analyses were almost coincided with each other. In addition, good agreement between the numerical and experimental stress distributions was also achieved. The stress at the position of the hoop strain gauge expressed the compressive characteristic, which was the same with that reported in experimental investigations. Hence, the proposed FE models could be used with confidence to predict the stress distributions of the bolted ball-cylinder joint.

3.3 Load-displacement curves

Load-displacement curves were adopted for the further understanding of the mechanical behaviour of bolted ball-cylinder joints. The displacement represented the deformation of the loading point at the hollow cylinder. The load-displacement curves of the bolted ball-cylinder joint specimens obtained from the FE simulations were validated with the experimental results and shown in Fig. 15. Moreover, the comparisons of the whole range characteristics, ultimate loads P_u and initial stiffness S_{in} of the bolted ball-cylinder joint specimens are summarized in Table 2 and Table 3, respectively.

It is found that the axial stiffness was responsible for the elastic behaviour at the beginning of the loading process. However, when the force became larger than a specific value, the plastic behaviour developed significantly. The main reason for this might be that a plastic hinge was created at the hollow cylinder. In the design of the bolted ball-cylinder joint, the force and the deformation were usually limited for the practical application. At the plastic phase, the joint deformation continued to increase rapidly with a small load increment. Therefore, the joint was not suitable for the further loading. At that time, the failure mode occurred.

From the load-displacement curves plotted in Fig. 15, it can be seen that the curves obtained numerically and experimentally were extremely close on the whole range characteristics. According to the ultimate loads listed in Table 2, good agreement between the experimental and numerical ultimate loads was achieved with the maximum deviation of 7.35%, minimum deviation of 1.1% and average deviation of 4.12%. The initial stiffness calculated by least square method (Wu *et al*. 2012) is listed in Table 3. It is noted that the maximum, minimum and average deviations of the initial stiffness between the test data and the FE prediction were 3.97%, 0.81% and 2.5%, respectively. Thereby, the proposed FE models predicted the whole range characteristics, ultimate loads and initial stiffness of all bolted ball-cylinder joint specimens very well.

On the basis of the FE data, it can be found that both the ribbed stiffener and the dimensions of the hollow cylinder had important effects on the mechanical behaviour of the bolted ball-cylinder joint: (1) the ribbed stiffener could improve not only the ultimate load, but also the initial stiffness; (2) the thicker hollow cylinder could achieve a better mechanical behaviour of the bolted ball-cylinder joint; (3) the larger outside diameter of the hollow cylinder weakened the initial stiffness of the bolted ball-cylinder joint.

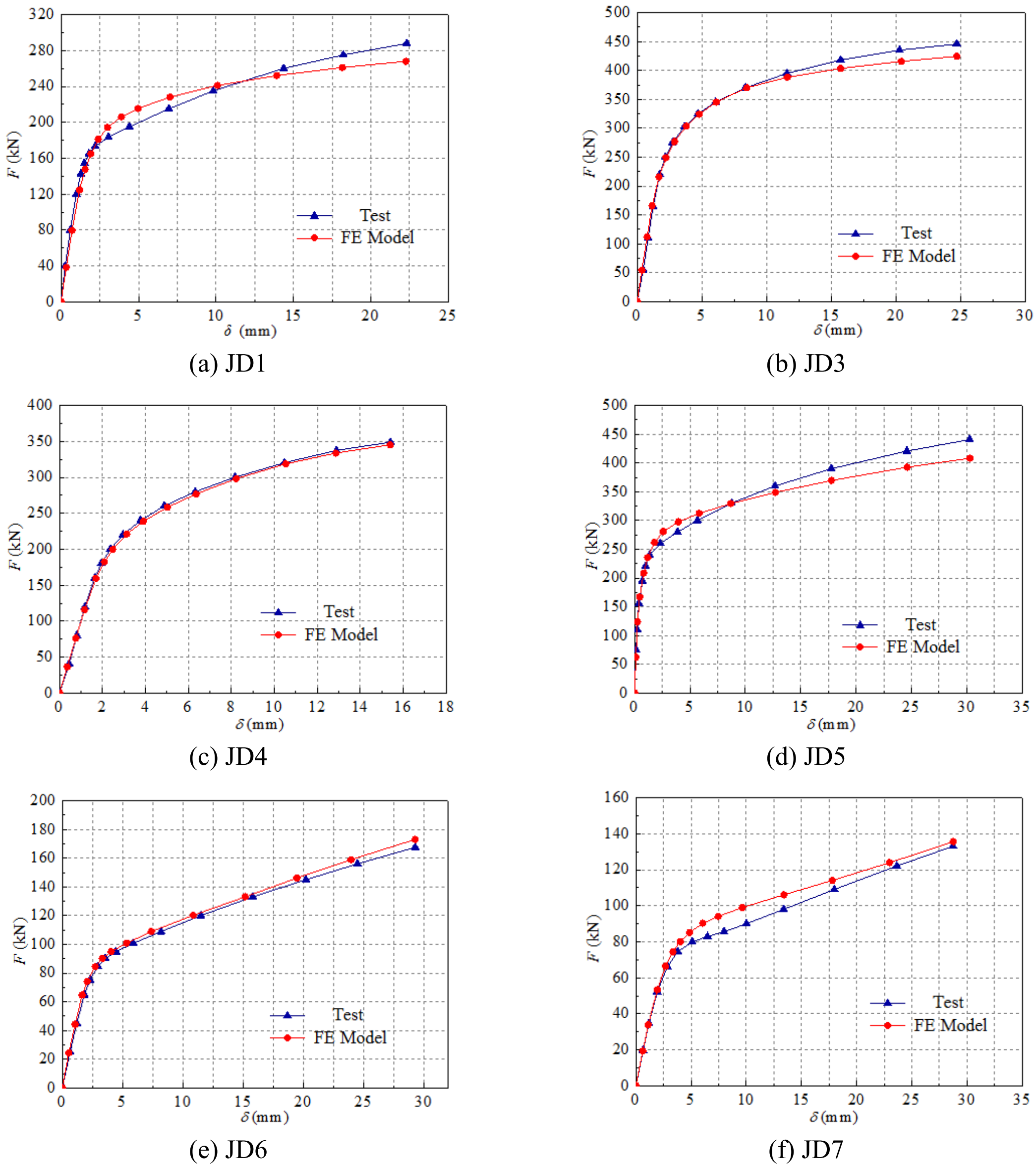

(a) JD1 (b) JD3

(c) JD4 (d) JD5

(e) JD6 (f) JD7

Fig. 15 Load-displacement curves

Table 2 Comparisons of ultimate loads

No.	$P_{u,\text{test}}$ (kN)	$P_{u,\text{FE}}$ (kN)	Deviation
JD3	446.00	424.45	4.83%
JD4	349.20	345.35	1.10%
JD5	440.60	408.29	7.33%
JD6	167.70	173.04	3.18%
Mean			4.12%

Table 3 Comparisons of initial stiffness

No.	$S_{in,\text{test}}$ (kN/mm)	$S_{in,\text{FE}}$ (kN/mm)	Deviation
JD1	104.07	100.71	3.23%
JD3	121.62	123.16	1.27%
JD4	96.13	92.31	3.97%
JD5	504.05	485.35	3.71%
JD6	34.40	34.68	0.81%
JD7	27.79	28.35	2.02%
Mean			2.50%

4. Parametric studies

In order to develop a further understanding of the mechanical behaviour of the bolted ball-cylinder joint and provide valuable data for the theoretical studies and engineering design, parametric studies have been performed by using the proposed FE models. A total of 35 bolted ball-cylinder joints with different practical parameters were analyzed in the parametric studies, as described in Table 4. The parameters included the outside diameter of the hollow cylinder d_1, the thickness of the hollow cylinder t, the height of the hollow cylinder H, the width of the rectangular tube b, the design length of the upper chord members L (the length of the rectangular tube was $L/2$-$d_1/2$ in the FE models), the width of the convex washer w_w, the thickness of the convex washer t_w, the width of the ribbed stiffener w_s and the thickness of the ribbed stiffener t_s. The initial stiffness S_{in} of these practical joint models was also provided in Table 4.

4.1 Effect of the outside diameter of the hollow cylinder

It has been recognized that the outside diameter of the hollow cylinder has a significant influence on the mechanical behaviour of the bolted ball-cylinder joint (Guo *et al*. 2016a). Four kinds of the outside diameters of the hollow cylinder with the magnitude of d_1 = 100 mm, 120 mm, 140 mm and 160 mm (BBCJ1~BBCJ4) were taken into consideration in the numerical modelling. Their load-displacement curves are plotted in Fig. 16. It is indicated that the ultimate load of bolted ball-cylinder joints decreased with the increase of the outside diameter of the hollow cylinder due to the reduction of the joint stiffness. When the outside diameter of the hollow cylinder increased from 100 mm to 160 mm gradually, the initial stiffness reduced by 40.9%, 53.3% and 58.8%, respectively. However, it is worth noting that the larger the outside diameter of the hollow cylinder is, the slighter its effect is.

Table 4 Characteristics of 35 FE models for parametric studies

Model	Hollow cylinder			Rectangular tube		Convex washer		Ribbed stiffener		S_{in} (kN/mm)
	d_1 (mm)	t (mm)	H (mm)	b (mm)	L (m)	w_w (mm)	t_w (mm)	w_s (mm)	t_s (mm)	
BBCJ1	100	8	130	50	4.8	36	6	None	None	148.01
BBCJ2	120	8	130	50	4.8	36	6	None	None	87.44
BBCJ3	140	8	130	50	4.8	36	6	None	None	69.18
BBCJ4	160	8	130	50	4.8	36	6	None	None	60.97
BBCJ5	120	8	90	40	3.2	30	5	None	None	72.64
BBCJ6	120	10	90	40	3.2	30	5	None	None	96.32
BBCJ7	120	12	90	40	3.2	30	5	None	None	139.85
BBCJ8	120	14	90	40	3.2	30	5	None	None	199.92
BBCJ9	120	10	100	50	4	30	5	None	None	131.22
BBCJ10	120	10	110	50	4	30	5	None	None	121.99
BBCJ11	120	10	120	50	4	30	5	None	None	116.32
BBCJ12	120	10	130	50	4	30	5	None	None	111.82
BBCJ13	140	12	110	40	4	30	5	None	None	116.2
BBCJ14	140	12	110	50	4	30	5	None	None	134.87
BBCJ15	140	12	110	60	4	30	5	None	None	158.99
BBCJ16	140	12	110	70	4	30	5	None	None	176.57
BBCJ17	100	8	90	40	1.2	30	5	None	None	85.23
BBCJ18	100	8	90	40	1.8	30	5	None	None	87.11
BBCJ19	100	8	90	40	2.5	30	5	None	None	90.3
BBCJ20	100	8	90	40	3.2	30	5	None	None	95.25
BBCJ21	160	12	150	70	5.6	36	8	None	None	145.89
BBCJ22	160	12	150	70	5.6	48	8	None	None	147.73
BBCJ23	160	12	150	70	5.6	54	8	None	None	148.26
BBCJ24	160	12	150	70	5.6	42	8	None	None	146.95
BBCJ25	160	12	150	70	5.6	42	4	None	None	143.3
BBCJ26	160	12	150	70	5.6	42	6	None	None	144.62
BBCJ27	160	12	150	70	5.6	42	10	None	None	148.96
BBCJ28	140	10	130	50	4.8	36	6	6	10	134.37
BBCJ29	140	10	130	50	4.8	36	6	12	10	226.08
BBCJ30	140	10	130	50	4.8	36	6	24	10	591.41
BBCJ31	140	10	130	50	4.8	36	6	None	None	83.42
BBCJ32	140	10	130	50	4.8	36	6	18	10	394.47
BBCJ33	140	10	130	50	4.8	36	6	18	6	281.85
BBCJ34	140	10	130	50	4.8	36	6	18	8	342.68
BBCJ35	140	10	130	50	4.8	36	6	18	12	442.74

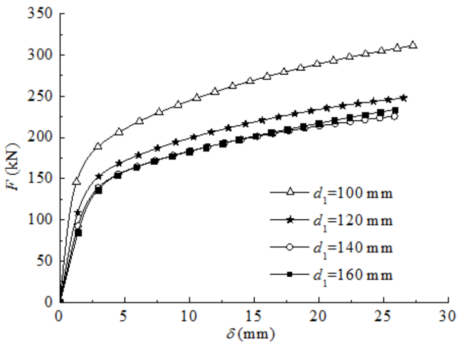

Fig. 16 Effect of the outside diameter of the hollow cylinder

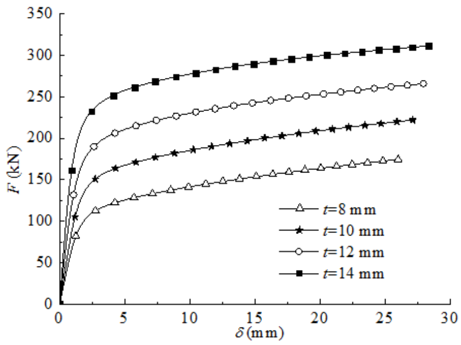

Fig. 17 Effect of the thickness of the hollow cylinder

4.2 Effect of the thickness of the hollow cylinder

The load-displacement curves of the joint models BBCJ5~BBCJ8 which only differ in the thickness of the hollow cylinder (8 mm, 10 mm, 12 mm and 14 mm) are shown in Fig. 17. It is found that compared with the initial stiffness of the joint model BBCJ5, the initial stiffness of the joint models BBCJ6~BBCJ8 improved by 32.8%, 92.5% and 175.2%, respectively. As expected, the bolted ball-cylinder joint with thicker hollow cylinder had a higher ultimate load.

4.3 Effect of the height of the hollow cylinder

Fig. 18 shows the effect of the height of the hollow cylinder on the load-displacement responses of the joint models BBCJ9~BBCJ12. Four different heights of the hollow cylinder of 100 mm, 110 mm, 120 mm and 130 mm were considered. It can be seen that the joint stiffness enhanced with the decrease of the height of the hollow cylinder, leading to the improvement of the ultimate load.

4.4 Effect of the width of the rectangular tube

From the theoretical point of view, the loaded rectangular tube could restrict the deformation of the hollow cylinder at the connecting region, when the bolted ball-cylinder joint was subjected to

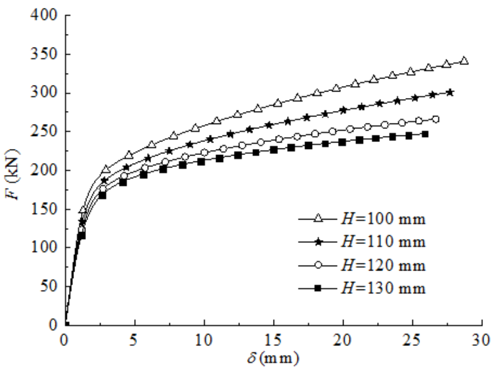

Fig. 18 Effect of the height of hollow cylinder

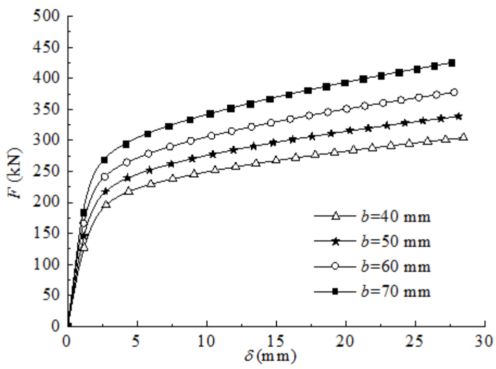

Fig. 19 Effect of the width of the rectangular tube

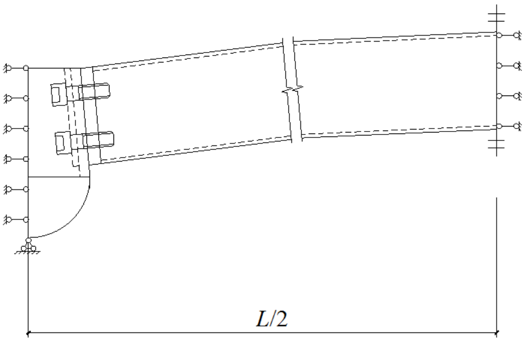

Fig. 20 Deformation of the compression joint

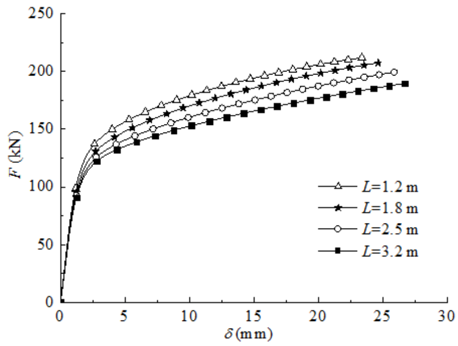

Fig. 21 Effect of the length of the rectangular tube

axial compressive load. The FE results are shown in Fig. 19 with four different widths of the rectangular tube of 40 mm, 50 mm, 60 mm and 70 mm (BBCJ13~BBCJ16). It can be observed that the increase of the width of the rectangular tube improved the mechanical behaviour of the bolted ball-cylinder joint. The primary reason for this may be that the wider rectangular tube reduced the deformation area of the hollow cylinder. As a result, both the joint stiffness and ultimate load improved.

4.5 Effect of the length of the rectangular tube

In the practical engineering, the deformation of the compression joint is shown in Fig.20. In general, the deformation of the hollow cylinder was in accordance with the bending deformation of the rectangular tube. Hence, the length of the rectangular tube had an effect on the mechanical behaviour of the bolted ball-cylinder joint. Four joint models BBCJ17~BBCJ20 which have different design lengths of the upper chord members (1.2 m, 1.8 m, 2.5 m and 3.2 m) were selected for this parametric analysis. The corresponding FE results are shown in Fig. 21. It is interesting to find that the length of the rectangular tube had a slight influence on the initial stiffness. However, when the joint behaviour entered into the plastic phase, the shorter rectangular tube improved the joint stiffness and ultimate load effectively. The main reason for this is that on one hand, the deformation of the hollow cylinder was small at the elastic phase, leading to the similar response of these four joint models. On the other hand, the deformation of the hollow cylinder became larger at the plastic phase. At that time, the shorter rectangular tube which has a greater bending stiffness limited the deformation of the hollow cylinder more effectively, resulting in the improvement of the joint stiffness and ultimate load.

4.6 Effect of the width and thickness of the convex washer

Figs. 22 and 23 show the influences of the width and thickness of the convex washer on the load-displacement curves of bolted ball-cylinder joints, respectively. Four values of the convex washer width of 36 mm, 42 mm, 48 mm and 54 mm (BBGJ21~BBCJ24) and four values of the convex washer thickness of 4 mm, 6 mm, 8 mm and 10 mm (BBCJ24~BBCJ27) were examined. It is found that the bolted ball-cylinder joint was not sensitive to the change of both the width and thickness of the convex washer. Therefore, these effects on the mechanical behaviour of bolted ball-cylinder joints were negligible.

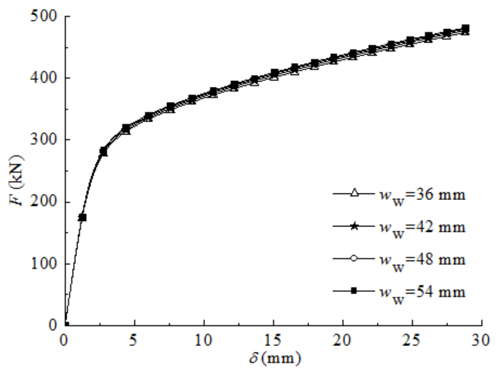

Fig. 22 Effect of the width of the convex washer

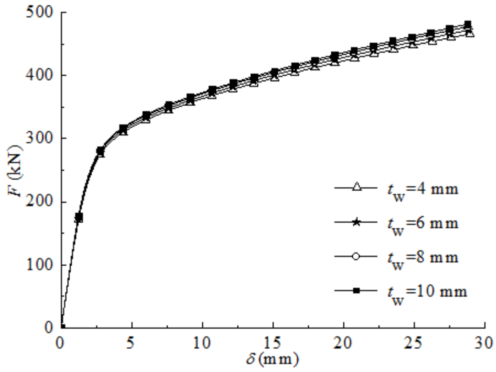

Fig. 23 Effect of the thickness of the convex washer

4.7 Effect of the width and thickness of the ribbed stiffener

To investigate the effects of the width and thickness of the ribbed stiffener on the mechanical characteristics of bolted ball-cylinder joints, eight joint models were established. Five of them (BBCJ28~BBCJ32) were different in the ribbed stiffener width of 0 mm, 6 mm, 12 mm, 18 mm and 24 mm, while five of them (BBCJ31~BBCJ35) varied in the ribbed stiffener thickness of 0 mm, 6 mm, 8 mm, 10 mm and 12 mm. Their load-displacement curves are plotted in Fig.24 and Fig. 25, respectively. It can be seen that (1) both the width and thickness of ribbed stiffener extremely improved the initial stiffness and ultimate load of bolted ball-cylinder joints; (2) the effect of the ribbed stiffener width was more outstanding than that of the ribbed stiffener thickness.

5. Conclusions

In this paper, the mechanical behaviour of the bolted ball-cylinder joint has been discussed via FE simulations. The main conclusions can be drawn as follows:

The proposed FE models successfully predicted the failure modes, stress distributions and load-displacement curves of the bolted ball-cylinder joint with sufficient accuracy, which implies that the proposed FE models have become an efficient tool to investigate the mechanical behavior of the bolted ball-cylinder joint.

The mechanical behaviour of the bolted ball-cylinder joint primary went through two phase: the elastic phase and the plastic phase. The generation of the plastic hinge signifies that the joint behaviour entered into the plastic phase.

The parametric studies were developed for the further investigation. (1) The ultimate load of bolted ball-cylinder joints decreased with the increase of the outside diameter of the hollow cylinder. (2) The bolted ball-cylinder joint with thicker hollow cylinder had a higher ultimate load and a higher joint stiffness. (3) In a rational range, the decrease of the height of the hollow cylinder led to the improvement of the ultimate load. (4) The increase of the rectangular tube width improved the mechanical behaviour of the bolted ball-cylinder joint. (5) The shorter rectangular tube resulted in the improvement of the joint stiffness and ultimate load. (6) The bolted ball-cylinder joint was not sensitive to the change of both the width and thickness of the convex washer. (7) Both the width and thickness of ribbed stiffener extremely improved the initial stiffness and ultimate load of bolted ball-cylinder joints. In addition, the effect of the ribbed stiffener width was more outstanding than that of the ribbed stiffener thickness.

Acknowledgments

The authors gratefully acknowledge the financial support provided by Natural Science Foundation of China under Grant No. 50908168 and No. 51478335. The authors would like to thank Linlin Liu for excellent technical support.

References

Bao, S.H. and Gong, T.Q. (2006), *Structural Mechanics*, Wuhan University of Technology Press, Wuhan, China.

Chen, Y., Feng, R. and Wang, J. (2015), "Behaviour of bird-beak square hollow section X-joints under in-plane bending", *Thin-Wall. Struct.*, **86**, 94-107.

Cheng, B., Qian, Q. and Zhao, X.L. (2015), "Numerical investigation on stress concentration factors of square bird-beak SHS T-joints subject to axial forces", *Thin-Wall. Struct.*, **94**, 435-445.

Ebadi, M. and Davoodi, M. (2012), "Evaluate Axial Stiffness of the MERO Connection, Under the Effect of Hardening the Screw", *Int. J. Sci. Emerg. Technol.*, **4**(1), 116-122.

Fan, F., Ma, H.H., Chen, G.B. and Shen, S. (2012), "Experimental study of semi-rigid joint systems subjected to bending with and without axial force", *J. Construct. Steel Res.*, **68**(1), 126-137.

GB 50017-2003 (2003), Code for design of steel structures; Ministry of housing and urban-rural development of the people's republic of China, General administration of quality supervision, inspection and quarantine of the people's republic of China. [In Chinese]

Ghasemi, M., Davoodi, M.R. and Mostafavian, S.A. (2010), "Tensile stiffness of MERO-type connector regarding bolt tightness", *J. Appl. Sci.*, **10**(9), 724-730.

Gil, B. and Bayo, E. (2008), "An alternative design for internal and external semi-rigid composite joints. Part II: Finite element modelling and analytical study", *Eng. Struct.*, **30**(1), 232-246.

Guo, X.N., Xiong, Z., Luo, Y.F., Qiu, L.Q. and Huang, W.J. (2015a), "Application of the component method to aluminum alloy gusset joints", *Adv. Struct. Eng.*, **18**(11), 1845-1858.

Guo, X.N., Xiong, Z., Luo, Y.F., Qiu, L. and Liu, J. (2015b), "Experimental investigation on the semi-rigid behavior of aluminium alloy gusset joints", *Thin-Wall. Struct.*, **87**, 30-40.

Guo, X.N., Huang, Z., Xiong, Z., Yang, S. and Peng, L. (2016a), "Experimental studies on behaviour of bolted ball-cylinder joint under axial force", *Steel Compos. Struct.*, *Int. J.*, **10**(1). [In press]

Guo, X.N., Xiong, Z., Luo, Y.F., Xu, H. and Liang, S.P. (2016b), "Block tearing and local buckling of aluminum alloy gusset joint plates", *KSCE J. Civil Eng.*, **20**(2), 820-831.

Hyde, T.H. and Leen, S.B. (1997), "Prediction of elastic–plastic displacements of tubular joints under combined loading using an energy-based approach", *J. Strain Anal.*, **32**(6), 435-454.

Leen, S.B. and Hyde, T.H. (2000), "On the prediction of elastic-plastic generalized load-displacement responses for tubular joints", *J. Strain Anal.*, **35**(3), 205-219.

Lesani, M., Bahaari, M.R. and Shokrieh, M.M. (2013) "Detail investigation on un-stiffened T/Y tubular joints behavior under axial compressive loads", *J. Construct. Steel Res.*, **80**(4), 91-99.

Loh, H.Y., Uy, B. and Bradford, M.A. (2006a), "The effects of partial shear connection in composite flush end plate joints Part I — experimental study", *J. Construct. Steel Res.*, **62**(4), 378-390.

Loh, H.Y., Uy, B. and Bradford, M.A. (2006b), "The effects of partial shear connection in composite flush end plate joints Part II—Analytical study and design appraisal", *J. Construct. Steel Res.*, **62**(4), 391-412.

Lopez, A., Puente, I. and Miguel, A.S. (2007), "Numerical model and experimental tests on single-layer latticed domes with semi-rigid joints", *Comput. Struct.*, **85**(7-8), 360-374.

Ma, H.H., Fan, F., Chen, G.B. and Shen, S.Z. (2013), "Numerical analyses of semi-rigid joint systems subjected to bending with and without axial force", *J. Construct. Steel Res.*, **90**, 13-28.

Pearson, I.T. and Mottram, J.T. (2012), "A finite element modelling methodology for the non-linear stiffness evaluation of adhesively bonded single lap-joints: Part 1. Evaluation of key parameters", *Comput. Struct.*, **90-91**,76-88.

Pena, A. and Chacon, R. (2014), "Structural analysis of diamond bird-beak joints subjected to compressive and tensile forces", *J. Construct. Steel Res.*, **98**, 158-166.

Qiang, X.H., Bijlaard, F.S.K., Kolstein, H. and Jiang, X. (2014), "Behaviour of beam-to-column high strength steel endplate connections under fire conditions - Part 2: Numerical study", *Eng. Struct.*, **64**, 39-51.

Qiu, G.Z. and Zhao, J.C. (2009), "Analysis and calculation of axial stiffness of tubular X-joints under compression on braces", *J. Shanghai Jiaotong Univ.*, **14**(4), 410-417.

Thai, H.T. and Uy, B. (2015), "Finite element modelling of blind bolted composite joints", *J. Construct. Steel Res.*, **112**, 339-353.

Wang, X., Dong, S.L. and Wang, H.Y. (2000), "Finite element analysis of welded spherical joints' stiffness", *J. Zhejiang Univ. (Engineering Science)*, **34**(1), 77-82.

Wu, J.M. (2012), "Least squares methods for solving partial differential equations by using Bézier control points", *Appl. Math. Comput.*, **219**(8), 3655-3663.

CC